Electrochimica Acta 580 (2026) 149933



Contents lists available at ScienceDirect

Electrochimica Acta

journal homepage: www.journals.elsevier.com/electrochimica-acta



Molecular dynamics simulations of Nafion thin films at a platinum catalyst surface: Correlating structure with charging behaviour☆

Dustin Vivod [a],*, Binny A. Davis [a], Tobias Binninger [a], Michael Eikerling [a,b]

[a] Theory and Computation of Energy Materials (IET-3), Institute of Energy Technologies, Forschungszentrum Jülich, 52425, Jülich GmbH, Germany
[b] Chair of Theory and Computation of Energy Materials, Faculty of Georesources and Materials Engineering, RWTH Aachen University, 52062, Aachen, Germany

ARTICLE INFO

Keywords:
Molecular dynamics
Catalyst–ionomer interface
Ionomer thin-film
Charged interfaces
Electrode potential
Differential capacitance

ABSTRACT

Electrocatalysis is greatly influenced by the local conditions at the catalyst-electrolyte interface, which are governed by the structure of the catalyst, the composition of the electrolyte, and the interfacial electric field. In catalytic systems comprised of complex molecular species like ionomers, the distribution of electrolyte can vary substantially, resulting in heterogeneous local reaction environments. In order to gain atom-scale insight into this micro-environment we construct a model system consisting of a platinum surface, varying levels of water, and a Nafion thin film and conduct molecular dynamics simulations. We employ a construction based on Voronoi tessellation to assemble a dense film of ionomer that fully covers the platinum surface. A first rough energy analysis reveals that water film configurations with thickness of less then 20 Å seem to be stable. Simulations with charged platinum surfaces are analysed in view of electrostatic conditions and differential capacitance of the interface configuration. Trends observed in these properties can be interpreted in view of the crowding of hydronium ions or the Nafion film at the platinum surface. The presented workflow can be easily applied to investigate novel ionomers for use in PEFCs.

1. Introduction

Electrochemical energy conversion devices such as fuel cells and electrolysers utilise nanostructured catalyst layers (CL) at which redox reactions take place to produce or consume oxygen and hydrogen gas, associated with the consumption or generation of electrical energy. To provide proton-conducting pathways to the surface of the electrocatalyst, at which the reactions proceed, and to improve the structural integrity of the CL, ionomer is added to it. In the specific case of polymer electrolyte fuel cells (PEFCs), the use of platinum as the catalyst and Nafion as the ionomer is well established and serves as the benchmark [1,2]. However, due to the cost of platinum and rising health concerns around per- and polyfluorinatedalkyl substances (PFAS), which Nafion is made of, new materials are sought after [3–6].

The microscopic interfacial region where the electrocatalyst and the electrolyte come together defines the local reaction environment (LRE). As the name suggests it comprises distributions of properties that determine the rates of electocatalytical reactions in the immediate vicinity of the catalyst, at atom-scale distance. Relevant properties include the structure and orientation of water molecules, ion densities, as well as the electrostatic potential or electric field. Small changes in any of these properties can induce pronounced variations in the rates of targeted reactions and degradation processes [7–9]. The importance of the LRE for the electrocatalytic activity has been discussed extensively in the literature [10–12]. It is shown that local effects such as cation and anion effects, and the local pH influence the electrocatalytic reactions greatly [13]. In the case of PEFCs, the distribution of Nafion around the platinum catalyst is known to exert a strong impact on device performance, as local transport processes are altered [14]. It is evident that in order to find replacements for catalyst and ionomer that yield required cost reductions, deliver gains in performance and stability, and alleviate environmental concerns, it is crucial to understand the LRE.

In the nano-confined region of the LRE, the properties of the electrolyte, such as the chemical potential or diffusion coefficient of water, as well as the concentrations and distribution of protons, differ strongly from those in the bulk due to the close proximity of the catalyst. Thus, the electric field and potential distribution in the confined electrolyte are also different. As such, the interface region that defines the LRE can exhibit a range of structures. One such structural motif that is being discussed in the literature is the presence and thickness of a thin water film between electrode and ionomer [15–17]. Recent studies by Chabot et al. used small-angle neutron scattering (SANS) to elucidate the structure of ionomer-bound interfaces in cathode catalyst layers of

☆ This article is part of a Special issue entitled: 'TheCAT25' published in Electrochimica Acta.

* Corresponding author.
E-mail address: d.vivod@fz-juelich.de (D. Vivod).

https://doi.org/10.1016/j.electacta.2026.149933
Received 31 March 2026; Received in revised form 22 August 2026; Accepted 6 September 2026
Available online 18 September 2026
0013-4686/© 2026 The Authors. Published by Elsevier Ltd. This is an open access article under the CC BY license (http://creativecommons.org/licenses/by/4.0/).
Open access funding enabled and organized by Projekt DEAL.

PEFCs, and thus provide valuable insight into the LRE [16,18]. They interpreted SANS data with the presence of a thin water film between a skin-type ionomer layer and the catalyst. The water film thickness they observed was in the range of 7–13 Å, while the ionomer layer was between 20–30 Å thick. These thicknesses varied depending on the relative humidity and the carbon support material that was used. The structural motif of this thin-film morphology is further supported by compelling intuitive arguments. It underpins the need for well-devised models that adequately represent the interface structure and conditions, and form a reliable basis for analyses of transport phenomena and reaction kinetics at the nanoscale.

Other works, including modelling and simulation studies, investigated the effect of a water film and its thickness on the LRE [17, 19–22]. These type of studies are vital, as experimental insights are difficult to obtain due to the nanoscale and complex nature of the LRE. A key benefit of these computational works is the possibility to investigate the influence of specific changes to a certain parameter such as water film thickness, ionomer structure or catalyst surface charge. Molecular dynamics (MD) simulations that investigate these influences have been carried out in studies that utilised a flat catalyst surface and a thin Nafion film that confine a water film of variable thickness. In simulations of Nouri-Khorasani et al., the concentration of protons located at the platinum surface was found to decrease with the increase in water film thickness [17]. Fernandez-Alvarez et al. on the other hand observed in their MD study that oxygen diffusion remains largely unaffected by a change in the water film thickness [19]. Both these MD studies provide atom-scale insight into spatial distributions of reactants. A key parameter that was evaluated in these studies is the charging state of the catalyst. As the surface charge at the catalyst varies with electrode potential during device operation, the effect of this charging has to be accounted for. The simplest way to achieve this is by adding charges *ad hoc* to the platinum atoms that remain fixed over the course of the simulation, corresponding to the fixed charged method (FCM). The more complex constant potential method (CPM), on the other hand, evaluates the point charges of a selected group of atoms at each time step at a set potential [23,24]. The CPM adds computational complexity with the argued benefit of being physically consistent. Zhang et al. compared the results for simulations of both FCM and the CPM using the otherwise same setup of a Nafion layer on a platinum surface [25]. However, with their setup they saw no change in the resulting electrostatic potential distribution. While the charging state was considered in these studies, the resulting electrostatic observables, such as the differential capacitance or the surface potential, were not investigated in full detail.

Other MD studies exist that have simulated the LRE in more complex systems of platinum nanoparticles supported on carbon with the Nafion phases created from annealing in order to bridge the gap to more realistic structures found in PEFCs [26–31]. However, due to the increase in complexity of these systems, the influence of specific parameters on the LRE is difficult to discern, thus they are more focused on investigating the transport properties of hydronium ions and the influence of the Nafion composition. For a more extensive review on the state of MD simulations of PEFCs we refer to a recent publication by Rayhani and Jian [32]. A physically coherent picture of the interplay of the interfacial water film with the properties of the ionomer film and the charging state of the catalyst jointly determining the electrostatic properties, is however still missing.

In this study, we utilise a thin-film structural model of an atom-scale thin slab of water that is confined between a planar platinum (111) surface and a quasi 2D skin layer of Nafion, thus resembling the layered structure identified by Chabot et al [16,18]. Our thin-film model uses freely moving strands of Nafion and is set-up with the help of Voronoi tessellation. Multiple systems are created that vary in water content to explore the effect of the water slab thickness, with the morphology of the water phase of our systems ranging from near-monolayer to bulk-like, with the Nafion side chains penetrating into the water phase. Changes to the charging state of the platinum surface are applied using the FCM. In this publication, we neglect the impact of the potential-dependent formation of chemisorbed oxygen species. The fixed charges imposed at the catalyst surface and at the ionomer skin are neutralised by adjusting the number of hydronium ions included in the simulations. The system is then investigated by complementary structural and electrostatic analyses. The structural analyses focus on providing an atom-scale picture of the LRE with varying water film thickness. We demonstrate how to obtain the differential capacitance we that deem of practical utility as a fingerprint of interface structured LRE.

Table 1
Approximate water film thicknesses in simulations of platinum-water systems at 298.15 K.

# Water molecules	Film thickness [Å]
1000	1.5
5000	13
9000	26

2. Computational details

MD simulations reported in this article have been performed using the LAMMPS [33] code for classical molecular dynamics simulation with force field (FF) parameters taken from previous publications [34, 35]. A cutoff of 12 Å was used for all interatomic potentials as well as for the direct part of the electrostatic interactions. Electrostatic interactions were calculated using the particle–particle–particle–mesh method with the slab correction and an accuracy of 10^{-5} eV Å^{-1} [36]. Periodic boundary conditions were employed in X and Y direction. A reflective wall has been added to all simulations at a distance of 60 Å away from the platinum surface. Any atom that would cross this wall is reflected back towards the platinum surface by flipping the sign of the velocity in Z direction. Simulations were carried out at temperatures of 298.15 K, i.e. room temperature (RT), and 353.15 K, controlled by a Nosé–Hoover thermostat with a damping constant of 0.5 ps. The time step for all simulations was 1 fs.

The platinum slab used was cut from the bulk crystal with a lattice constant of 3.94 Å. The surface of the slab had (111) orientation and the slab consisted of 9 layers. During the simulations the bottom 3 layers of the slab were frozen. The dimensions of the slab were 99.11 × 100.1 × 18.93 Å^3. The complete simulation cell consisted of the platinum slab on one side and a constraining deprotonated Nafion layer on the other side with the space in between filled with varying amounts of water molecules, namely 0, 1000, 5000, and 9000 water molecules. The systems are charge neutralised by addition of hydronium molecules. While the system with 0 water molecules is not physically motivated, since in this case the Nafion side chains would not be deprotonated, it is nevertheless used as a reference model system in the present computational study. By simulating the deprotonated Nafion side chains in this way the only differences arise from the added water molecules, and not from differences in the force field of the protonated and deprotonated side chains. In the first step the systems with only platinum and water were constructed and equilibrated for 6 ns at both RT and 353.15 K under NVT conditions. The resulting approximate water-film thicknesses are listed in Table 1

2.1. Nafion layer setup

To construct a dense Nafion film that covers the entire platinum slab, we proceed by first constructing auxiliary thin-film models of low density. To this end, a Nafion strand was created with five monomer repeat units (cf. Fig. 1). The oligomer strand has an equivalent weight of 1122 g mol^{-1}, which closely resembles the chemical composition

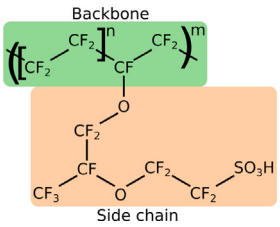


Fig. 1. Chemical structure of Nafion with backbone and side-chain parts highlighted in green and orange, respectively. In this study n=7 and m=5.

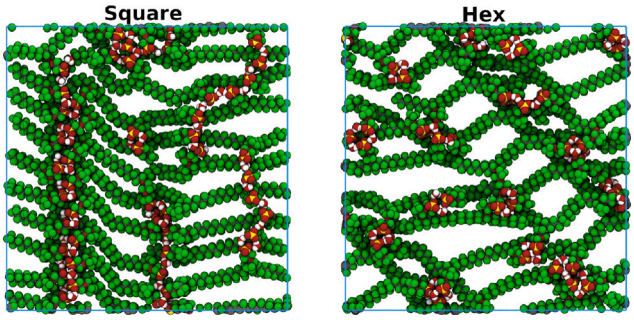


Fig. 2. Exemplary snapshots of the two initial Nafion layers used within this work. Hydronium ions were added for charge neutrality. Colour code: H: white, C: black, O: red, F: green, S: yellow. Note the accumulation of hydronium ions at the sulfonate groups.

of Nafion 117 as the most commonly variant used in PEFCs [37]. The strand was stretched in X direction to fit the dimensions of the Pt slab used. The stretched strand is replicated to construct the thin film. With this strand two different thin-film types were assembled. For the first type denoted as 'square' the strand was replicated in Y direction with a shifting vector of length 10 Å. The other, denoted as 'hex' was created by shifting of the strand in Y and X by 10 Å in both directions. The resulting layers, each consisting of 10 strands, are shown in Fig. 2. The number of strands was chosen such that the initial strands do not overlap. All sulfonic acid head groups were deprotonated, and as a result the Nafion molecules carried a negative charge. To ensure charge neutrality, the corresponding number of hydronium ions (H_3O^+) was added to the simulation cell.

These layers were added atop the platinum-water systems created before. The combined systems were simulated for a minimum of 5 ns. To verify that equilibration had been achieved, the total energy was monitored over the last 5 ns of simulation time. The data set was split into two halves, and a histogram was constructed for the energies of each set. The histograms were fitted via Gaussians, and equilibration was considered to be achieved when the difference between the two peak centres was less than 1% from one another, this value has been chosen to confirm that the fluctuations are consistent with thermal noise and that no systematic drift is present. After this equilibration, production runs of up to 40 ns of total simulation time were performed. The total simulation time needed was determined by the contacts of hydronium ions with the platinum surface (cf. SI Fig. 1), with simulation times being increased as long as an increase in contacts was observed. The block standard error of the potential energy for all simulations was less then 0.4 eV and the RMSDs of the positions of the Nafion backbone was less then 2 Å, indicating stable energies and conformations.

Afterwards, we performed Voronoi tessellations of the square and hex Nafion layers of all interface systems to rationalise a dense thin film of Nafion that uniformly covers the platinum slab. The Voronoi tessellation as implemented in SciPy generates a diagram of areas surrounding a set of given data points in 2D space [38]. Each point within a given area is closest to the data point, around which the area was constructed.

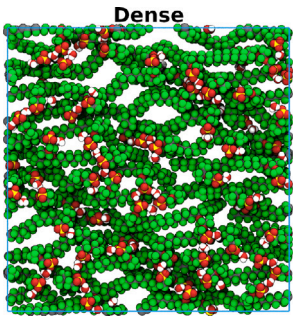


Fig. 3. Exemplary snapshot of the dense Nafion layer. Hydronium ions were added for charge neutrality. Colour code: H: white, C: black, O: red, F: green, S: yellow.

By taking the X and Y coordinates of the Nafion backbone carbon atoms as data points we interpret the area surrounding each data point as the spatial demand of the atom. As the Z coordinate is neglected, it has to be noted that errors are introduced in cases where backbone atoms overlap. For each trajectory, the Voronoi tessellation was performed at each frame, which are written every 1 ps, (cf. SI Fig. 3–6), and the minimum, maximum and median area sizes are noted (cf. SI Tab. 1). With the mean median area sizes collected from all trajectories, we estimate the number of Nafion strands necessary to cover the platinum slab. Dividing the area of the platinum slab (99.2 nm^2) by the mean median area of a single carbon backbone atom (0.106 ± 0.0088 nm^2) gives us the number of backbone carbon atoms (1020) that would fit onto the surface, within reasonable error. We have used a value of 0.0972 nm^2, that is one standard deviation lower than the average, as the area per backbone carbon in order to circumvent introduced errors due to the 2D projection. As the used Nafion strands contain 77 backbone atoms each, our simulation cell required 14 Nafion strands to completely cover the platinum surface. The resulting Nafion layer, depicted in Fig. 3, is called 'dense' and constructed by shifting the original strand by 10 Å in X and 7.5 Å in Y. The layer was then used to construct eight simulation cells with the platinum slab described above and 0, 1000, 5000, and 9000 added water molecules (cf. Fig. 5) at RT and 353.15 K with the same equilibration and production run protocol as detailed above. Fig. 4 shows the Voronoi tessellation for the dense layer of the simulation with 9000 added water molecules at 298.15 K, as well as the median backbone carbon area over the production run, and the distribution of area sizes. The plots verify a uniformly spread and that a stable Nafion film is present throughout the simulation. All further discussed simulations used this skin layer.

In order to compare the total energies of the platinum-water-Nafion systems, two additional simulations of pure water were carried out, one for each temperature considered here. These water systems contained 12000 water molecules and were exposed to periodic boundary conditions in all cardinal directions. The simulations were performed under NPT conditions using the Nosé–Hoover barostat with a damping constant of 5 ps and a target pressure of 1.01325 bar. They were equilibrated for 5 ns after which production runs of 5 ns were carried out, of which the energies where sampled.

2.2. Electrostatic potential and differential capacitance

By removing or adding hydronium ions to the system, a charge imbalance was created which was compensated by tuning the total charge of the surface Pt atoms (e.g., from 0 for the initial systems to +10 e, corresponding to ~0.007 e per surface platinum atom, for systems with 10 hydronium ions removed from the electrolyte slab).

In order to evaluate the capacitance of the interface, we first need to calculate the electrostatic interface potential. We start, analogous to

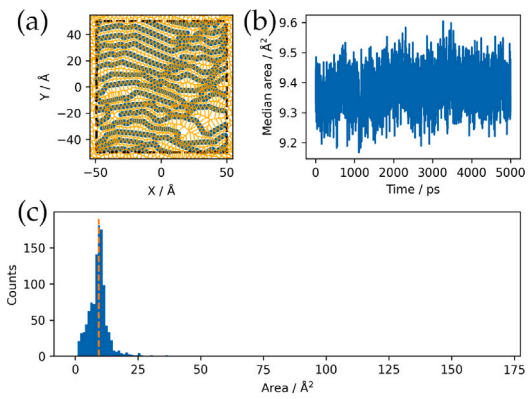


Fig. 4. Example of the Voronoi analysis for the dense Nafion layer with 9000 added water molecules at 298.15 K. (a) shows the averaged carbon backbones in blue and the resulting Voronoi diagram in orange, the black dashed lines indicate the simulation box. The median area size for each frame is shown in (b). The distribution of area sizes of the averaged Voronoi diagram is plotted in (c), with the orange dashed line marking the median.

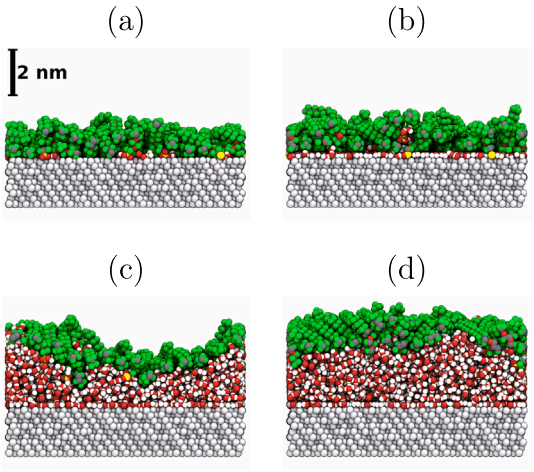


Fig. 5. Snapshots during production runs of systems with different water content. (a): 0 water molecules, (b): 1000 water molecules, (c): 5000 water molecules, (d): 9000 water molecules. Colour code: H: white, C: black, O: red, F: green, S: yellow, Pt: silver.

Lin et al. [39], from the Poisson equation,

$$\nabla^2\phi = -\frac{\rho}{\epsilon_0}, \tag{1}$$

where ϕ is the potential, ρ is the total charge density (including electrolyte species, vis. including solvent ions, as well as polymer constituents), and ϵ_0 is the vacuum permittivity. Since our system is 2D periodic in X and Y, and the interface spans along Z, we average the charge density in the X-Y-plane and rewrite Eq. (1) as

$$\frac{d^2\phi(z)}{dz^2} = -\frac{\rho(z)}{\epsilon_0}, \tag{2}$$

where $\rho(z)$ is the average charge density in the X-Y-plane and $\phi(z)$ the electrostatic potential at position z. Integrating Eq. (2) leads to

$$\phi(z) = -\frac{1}{\epsilon_0}\iint \rho(z)dzdu \tag{3}$$

The two integration constants in Eq. (3) are fixed by setting the potential and electric field to zero at z = ∞, which in our case corresponds to the edge of the simulation box at the maximum Z value Z_{max}. Thus, the potential is integrated from the vacuum side, starting from a value of 0, going through the Nafion layer, water film, and finally the platinum slab (cf. Fig. 5), yielding the upper integration bound of the minimum Z value Z_{min} of the simulation box. We evaluate the potential with respect to a vacuum reference and not with respect to an electrode reference as is oftentimes found in literature [25,39]. While this choice has no effect on the numeric results, it offers better insight from plots of the potential distribution. The difference in electrostatic potential between the platinum surface and the reference point is the surface potential ϕ_s, which is equivalent to the electrode potential. If a different vacuum reference was used, the resulting surface potentials would simply shift accordingly. The electrode potential of the uncharged simulations can then be related to the experimentally obtained electrode potential at the point of zero charge (PZC) found in literature. For a platinum (111) electrode the PZC is ~0.23 V vs. SHE [40]. Since the surface potentials are calculated from the spatial distribution of the atoms they are insensitive to the used simulation box and the used reflective wall. The spatial distribution of the atoms may be affected by the slab correction that has been employed, here we used the recommended value of 3 Å that is known to result in accurate dynamics.

The Pt surface was charged uniformly by fixed charges. Zhang et al. compared the difference of the fixed charge method (FCM) with the constant potential method (CPM) for a similar Pt-Nafion interface, where the Nafion was randomly dispersed and annealed atop the platinum surface [25]. In their evaluation, both methods led to similar results, with the FCM being much less computationally intensive. Thus we also use the FCM in our study. We consider 10 different surface charges ranging from −0.5 to 0.5 e nm^{-2} with a step size of 0.1 e nm^{-2}. The extra charges are balanced by adding or removing hydronium ions, where 10 hydronium ions correspond to a charge of ~0.1 e nm^{-2}, thus changing the topology of the system. To evaluate the effect of this change, each system was propagated for 1 ns during which the electric surface potential was calculated by averaging over windows of 100 ps. With this, we could verify that the potentials were equilibrated within ~0.5 ns (cf. SI Fig. 8). The number of hydronium ions with a distance of less then 4 Å also confirms stable configurations on average (cf. SI Fig. 9). Only simulations with 5000 added water molecules and negative surface charges show a slight increase in hydronium ions in close proximity over the last 0.5 ns, with a maximum average increase of 5 hydronium ions for simulations with a surface charge of −0.5 e nm^{-2}, which accounts for only 4.2% of all hydronium ions. We thus used the last 0.5 ns for analysis of the averaged charge densities and potentials. Each system was set up 3 times using different random number seeds for hydronium insertion or deletion, and the average charge densities are used for analysis. To further rationalise the usage of the FCM we have performed a singular set of simulations for the system with 1000 water molecules using the constrained charge ensemble [41] (cf. SI Fig. 10). In these simulations the point charges of the topmost platinum atoms are allowed to fluctuate during the simulation, with their total charge being constant. The individual charges are changed such that the energy is minimised. The resulting electrostatic potentials are comparable to those acquired with the FCM.

The differential capacitance was calculated via, the following relation,

$$C_{\mathrm{diff}} = \frac{\Delta\sigma}{\Delta\phi_s}, \tag{4}$$

where $\Delta\sigma$ is the change in surface charge between adjacent simulated charge states (in our case it is a constant value of 0.1 e nm^{-2}), and $\Delta\phi_s$ is the corresponding change in electric surface potential. The reported differential capacitances are calculated by considering the increase and decrease in surface charge for each data point and taking the average. The use of different vacuum reference would have no influence on the differential capacitance due to the derivative used in Eq. (4)

Structural analyses were carried out using MDAnalysis and VMD was used to render the figures of the simulation cells [42–45]. Unless

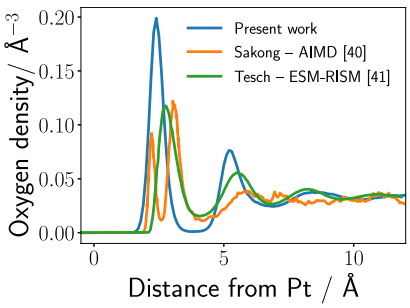


Fig. 6. Density distributions of water oxygen from different levels of theory [46,47].

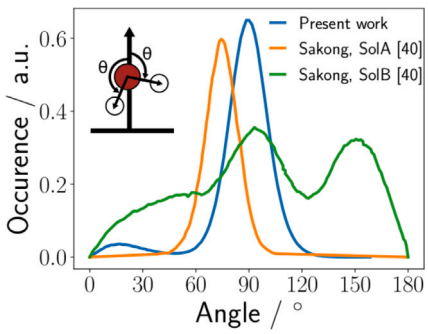


Fig. 7. Distributions of water OH bond angles to surface normal from this study (blue) and AIMD data (orange, green) taken from Ref. [46].

stated otherwise, only the last nanosecond of each trajectory was used for analysis.

3. Results and discussion

3.1. Force field validation

We assess the used FF in terms of its ability to adequately represent the structure of water in contact with the platinum surface under uncharged conditions. This interface has been investigated in multiple studies with various computational approaches, including *ab initio* MD (AIMD), which offers accurate atomic scale insight with which we can compare our results [46,47]. We find that the distribution of oxygen atoms of water from our simulations is in good agreement with literature results, as shown in Fig. 6. The AIMD simulations of Sakong and Groß yielded a water configuration with a double peak feature between 2–4 Å away from the surface [46]. Our results, as well as the results of Tesch et al. obtained using the effective screening medium-reference interaction site method (ESM-RISM) without treating water molecules in the first adsorption layer explicitly, do not show this feature [47]. Comparing the position of the peak closest to the Pt surface, we note that the one obtained in our studies is slightly closer to the surface compared to the other studies. The utilised force field slightly overestimates the adsorption of water onto the Pt surface, which we will take into consideration for the main results of the presented work.

Sakong and Groß also analysed the orientation of the water molecules that are less than 4 Å away from the platinum surface. They analysed the populations corresponding to the two peaks in Fig. 6 separately. The population belonging to the closest peak is denoted as SolA, the one belonging to the second peak as SolB. Adopting their analysis method of calculating the angle between the OH bonds with the surface normal, we compare the orientation of the molecules with a distance of less than 4 Å from the surface found in our simulations to their distributions in Fig. 7. In our simulations, the water molecules adsorb in a flat configuration as indicated by the main peak around 90°. The small second peak that is located at around 17° indicates a few hydrogen atoms are pointing towards the second water layer. The second peak of the SolB data around 150°, corresponding to hydrogen atoms that point towards the platinum surface, is not observed in our data. With this analysis we note that care has to be taken in interpreting structural information for the direct adsorption layer atop the platinum surface obtained with the used FF. Since the validation was done for the uncharged Pt-water system, the interpretation for the charged systems in Section 3.4 has to consider the higher adsorption strength between the platinum surface and water molecules, and the missing water layering. As a result the reorientation of the adsorption layers upon charging will be affected. Furthermore, more systematic overadsorption of different species is to be expected from systematic issues of the force-field fitting procedure.

3.2. Structural analysis of the Pt–water–Nafion interfaces

As the first analysis step of the platinum-water-Nafion systems, we turn towards the structural features of the systems. Fig. 8 shows the Z-density profiles of sulfur and backbone carbons of Nafion, as well as the profiles for the oxygen atoms of the hydronium and water molecules. For the sulfur atoms, we observe a peak close to the surface for all simulations except those with 9000 water molecules added, showing that there is contact between the platinum surface and the Nafion sulfo groups for the systems with a small number of water molecules. A second peak is observed for simulations with 5000 added water molecules at both temperatures. In the case of the simulation with 5000 added water molecules at RT the peak height of the second peak is even higher than the first. From the snapshot of this system in Fig. 5 and SI Fig. 11, we can see that the two peaks are caused by modulations that render some strands of the Nafion layer closer to the platinum surface than others. The waviness of the ionomer thin film in the X-Y plane is a result of the intricate interactions at play at this interface. The water is bound on one side by the platinum and on the other side by the Nafion strands, whose backbone is highly hydrophobic. Therefore, the area between water and the Nafion backbone is minimised during the simulation. Additionally, the potential energy of the sulfo groups that are less then 4 Å away from the surface is, on average, lower then those of the sulfo group further away, -0.23 ± 0.2 eV and 1.2 ± 0.2 eV, respectively. This indicates preferential adsorption of the sulfo groups. Due to the setup the water phase is however bound between the Nafion film and platinum surface, and thus the amount of sulfo groups that can adsorb is limited.

The density profiles of backbone carbon atoms show the expected behaviour of the Nafion layer being more separated from the platinum surface with increased water content. In simulations with 5000 added water molecules, the distributions are broader compared to the other simulations, which is a direct result of the wavy structure described above. For the density profiles of the hydronium oxygen atoms we notice that in all cases the first large peak is located in close proximity to the platinum surface, indicating a strong attraction of the hydronium ions to the surface. The temporal evolution shows that the number of ions at the platinum surface steadily increases with time in all simulations (SI Fig. 1). The adsorption strength is higher then the added energy due to thermal fluctuations, as the peaks are comparable between the different temperatures investigated. Due to the increased mobility of the hydronium ions at elevated temperatures more ions can get trapped in an adsorbed state at the surface. This strong interaction of the hydronium ions with the platinum surface was ascribed to polarisation of the metal surface due to the charged hydronium ions by Brunello et al. when they fitted the FF [35]. The presence of hydronium ions close to the platinum (111) surface is also supported by AIMD simulations, where spontaneous formation of hydronium in the water film less than 5 Å away from the platinum surface has been observed [48].

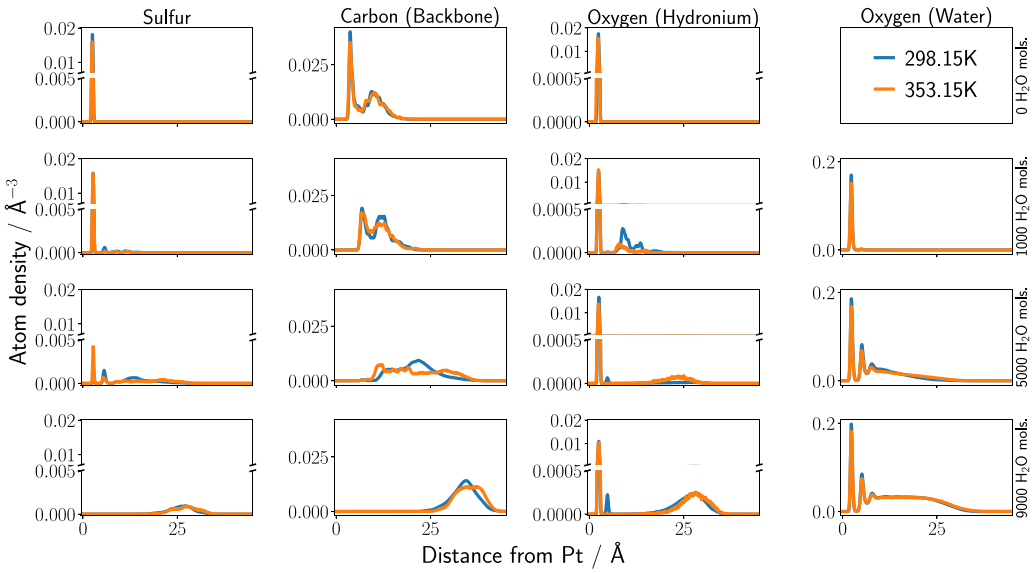


Fig. 8. Densities along Z direction from the Pt surface for selected atom species (column wise) of the 'dense' layer with different amounts of added water molecules (row wise). Note the broken axes in columns 1 and 3.

In their work, Sakong and Groß observed hydronium ions with a population probability of 10% per time step [48]. For a system with an implicit HCl concentration of 0.1 mol/L, Tesch et al. also observed hydronium ions near the platinum surface at the PZC [47]. In the latter work, the first adsorption layer had an increased concentration of ~0.113 mol/L. With an increase in the applied potential, the density of hydronium ions near the surface diminishes. As simulations discussed so far use an uncharged platinum slab they can be regarded as being performed at the PZC. Thus, the accumulation of hydronium ions is appropriate, however, the fact that ~70% of the hydronium ions are within 4 Å from the surface is not justified by DFT data in literature and can be regarded as overestimated due to utilised FF. The distribution of hydronium ions is governed by its chemical potential, which in turn differs spatially in the heterogeneous environment sampled in our systems [49]. As the Pt-hydronium interaction might however be overestimated, a true interpretation is not possible at this stage, as solvation effects and the electrostatic interactions, which would alter the adsorption energy, are likely underestimated. The density plots of the water oxygen atoms show only a single peak when 1000 water molecules are added, relating to only a singular water layer at the surface. The peak height is comparable to that of the first peak of the plots with higher water content. In the case of 5000 added water molecules, we see two additional peaks as well as a tail that extends to ~27 Å. Adding further water molecules extends this tail end to ~35 Å from the surface. While these values show the maximum distance to the surface where water is present they are not a direct value of the water film thickness, as the Nafion layer is extending into the water film as well. To provide a more detailed picture of the 2D water film thickness we have analysed the density of the water oxygen atoms further. Here, the density is calculated as the number density of oxygen atoms in a voxel-based grid with edge size of 0.5 Å throughout the simulation cell. Fig. 9 shows the maximum Z coordinate of the voxel in the X-Y bin that has a density above 0.0005 $Å^{-3}$, this value was chosen by visual inspection. From the maps we can see that the water film is patchy in the case of 1000 added water molecules. In these simulations the Nafion film is in direct contact to the platinum surface, indicated by the white areas where no water is present long enough. The hydronium ions that adsorb to the platinum surface also block the water molecules. With 5000 added water molecules, the water film thickness differs throughout the simulation cell. For both temperatures, we see spots that are not occupied by water, there the sulfo groups are adsorbed to the surface as seen in SI Fig. 11. For the simulations with

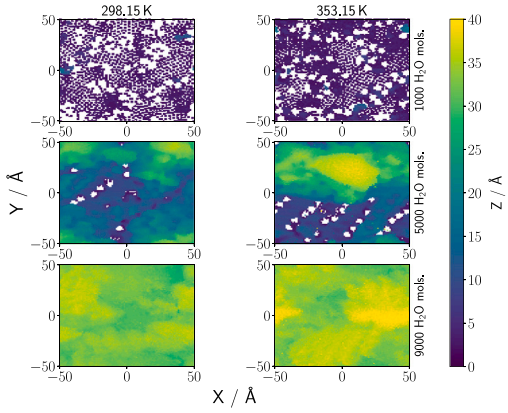


Fig. 9. Water film thickness for the different water contents (row wise) and temperatures (column wise). The colour denotes the maximum Z position for the given X-Y bin above a threshold of 0.0005 $Å^{-3}$, with white indicating no voxel above the threshold.

9000 added water molecules, the water film thickness is homogeneous as the Nafion film is completely separated from the platinum surface. The separation due to the increase in water content is enforced by our simulation setup, to study the preferential water film thickness later. In experiments, Berlinger et al. showed that an increase in water content in the catalyst ink leads to higher Nafion adsorption [50]. As we have seen, the potential energy of the sulfo groups is lower when in contact with the platinum surface, additionally the adsorbed hydronium ions at the platinum surface create a layer of positive charge that pulls the Nafion towards the surface, matching the experimental observations. The full hydrophobic interactions between the water and Nafion backbone that may drive the Nafion towards adsorption are not captured by our thin film setup, and warrant a different model [26].

In preparation for the following electrostatic investigation we analyse the equilibrium dipole fluctuations within the water phases for the different water contents at 298.15 K. In Fig. 10, we depict the slab-resolved dipole-covariance maps of the water molecules for the three water containing systems [51]. The plots show the covariance between the total water dipole components of water slabs with 1 Å thickness along the surface normal. The in-plane and surface-normal maps vary

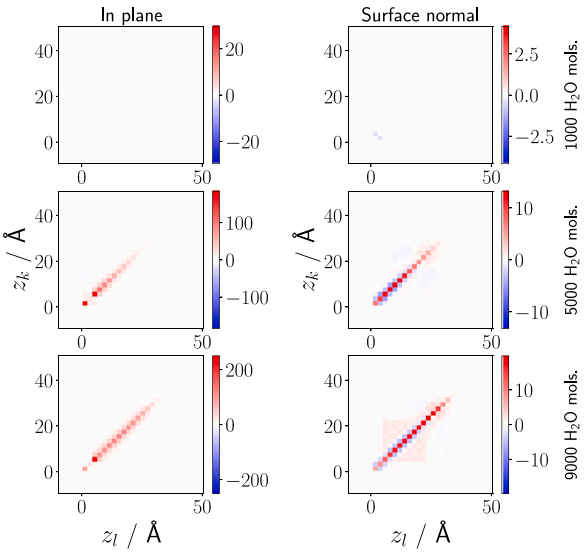


Fig. 10. Slab-resolved water dipole covariance maps for the water containing systems at 298.15 K. The results for the different water contents are shown row-wise. The axis denote the compared slabs (l and k) by their Z-distance to the platinum surface. The columns show the covariance of the in-plane and the surface-normal part of the water dipole, respectively. The colour bars show the dipole covariance in $e^2Å^2$.

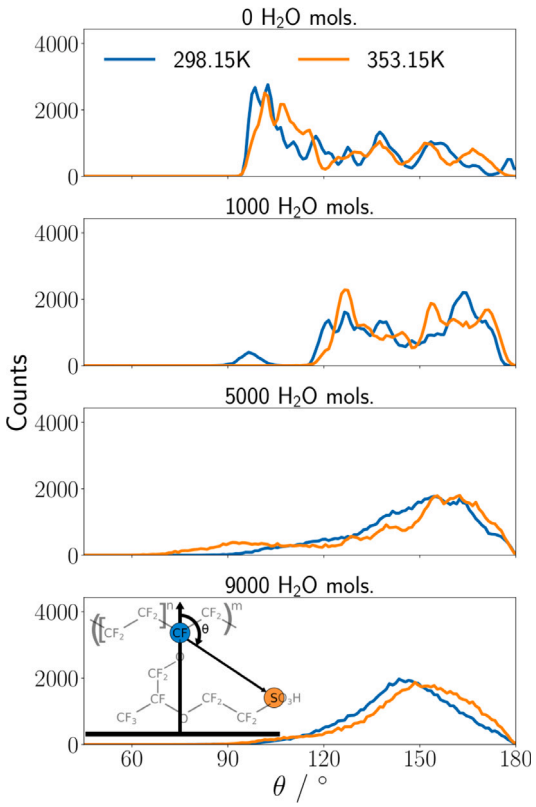


Fig. 11. Side-chain angles histograms of the 'dense' layer systems with different water content.

greatly in magnitude indicating an anisotropic polarisation response. The off-diagonal values show nonzero values, including negative ones, indicating coupling between the water layers. With these two observations, a strictly local and uniform dielectric description is inconsistent on the microscopic level [52].

A key structural feature of Nafion at the catalyst interface is the orientation of the side-chains with respect to the surface. Here, we describe the orientation via the angle between the vector from the carbon atom that connects to the side-chain to the sulfur atom of the side-chain, and the catalyst-surface normal (cf. SI Fig. 2). The resulting angle distributions are shown in Fig. 11. We observe that the side-chains tend towards a downward orientation to the surface with increased water content. Without added water, the distributions are spread over a broad range from 100° to 180°. As more water is added between the platinum surface and the Nafion thin film, this range narrows slightly to 120–180°. For the systems with 5000 and 9000 added water molecules, the maxima of the angular distributions are at ~160° and ~150°, respectively, showing a preference of the side-chains to be orientated towards the platinum surface.

Another key observation is that the shape of the distribution curves becomes smoother with an increase in water content. As the Nafion side chains are in direct contact with the surface in the low water content systems (cf. Fig. 8) they are less mobile, and the range of angles a specific side chain can explore during the simulation is constrained.

3.3. Estimating equilibrium water layer thickness

Utilising the energies of the different systems obtained during simulations, the equilibrium water film thickness can be estimated. The favourable water content can be estimated by relating the total energies E of two systems A and B with water contents W_A and W_B, where W_B is larger than W_A via

$$\Delta E = \frac{E_B - \left(E_A + ((W_B - W_A) \cdot E_{H_2O})\right)}{W_B - W_A}, \quad (5)$$

where E_{H_2O} is the energy of a water molecule obtained from simulations of bulk water. With the normalisation per water molecule, it can be considered an approximation for the chemical potential of water, where instead of the insertion of one molecule the average of 1000 or 4000 molecules is considered. The energy differences for the specific systems used in this study, as listed in Table 2, show a minimum for both temperatures when 1000 water molecules are added into the dry system. This minimum energy is negative indicating, that the solvation of the system is energetically favoured. If more water is added, the energies become positive indicating instability of the water film of our specific systems. It is reasonable to assume that the various solvation energies, e.g., water-Pt and water-ion, as well as the electrostatic double layer interactions lead to these changes. With this simplified analysis it is however not possible to distinguish between these contributions. From the explored water ranges we can draw a rough preliminary conclusion that a stable water film of less then 20 Å, comparable in thickness to the experimental values of Chabot et al. [18], forms in the gap between platinum and Nafion. By performing a more systematic computational study of the effect of varying the amount of water on the stability of the film, more precise values of the water film thickness will be obtained. Using grand canonical methods will allow the inclusion of entropic effects so far not considered [53].

Table 2
Difference in energy per water molecule of the systems w.r.t. to the system with the next lower water content, calculated with Eq. (5).

Water diff.	ΔE [eV H_2O^{-1}]	
	298.15 K	353.15 K
1000–0	−0.634 ± 0.010	−0.717 ± 0.014
5000–1000	0.0225 ± 0.003	0.0285 ± 0.004
9000–5000	0.0375 ± 0.004	0.0338 ± 0.006

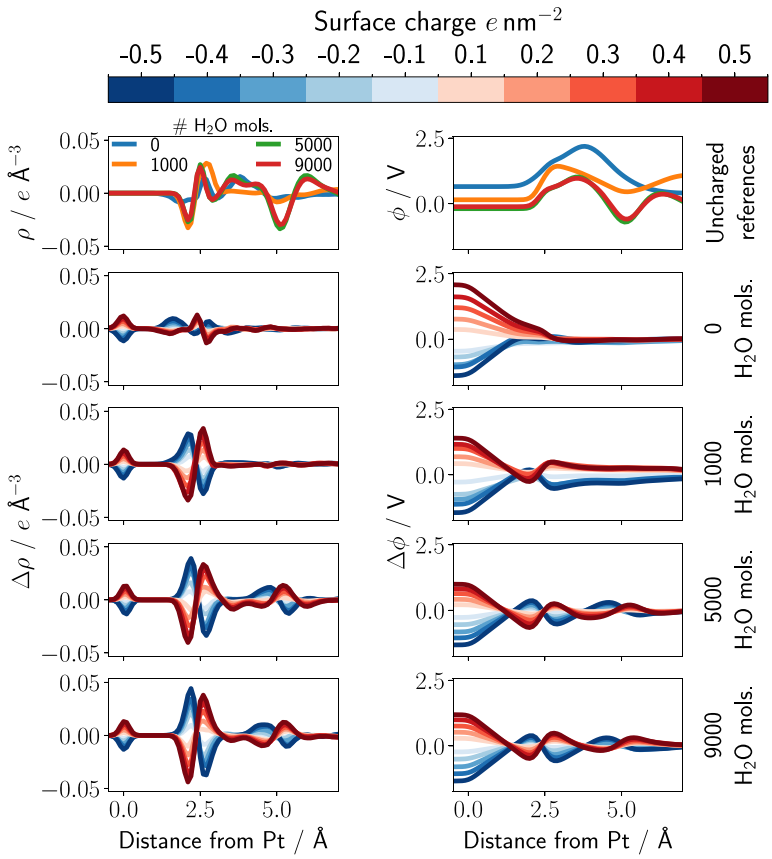


Fig. 12. Comparison of charge densities (left) and electrostatic potentials (right) between uncharged and charged systems. Top row are references from the uncharged simulations for each water content. Rows 2–5 are differences in charge density ($\Delta\rho$ (left)) and potentials ($\Delta\phi$ (right)) between the charged systems and the uncharged reference for 0, 1000, 5000 and 9000 added water molecules, respectively.

3.4. Electrostatics

After evaluating the structural features and water layer thickness of the uncharged system, we also investigate the effect of the water content on the electric surface potential of the platinum slab. The potential is calculated as described in the methods section for both uncharged systems and systems with a charged Pt surface.

The difference in charge densities and potentials of the charged simulations with respect to the uncharged ones are shown in Fig. 12, with:

$$\begin{aligned}\Delta\rho(z) &= \rho^{chg}(z) - \rho^{0}(z)\\ \Delta\phi(z) &= \phi^{chg}(z) - \phi^{0}(z),\end{aligned} \tag{6}$$

where $\rho^{chg}(z)$ and $\phi^{chg}(z)$ are the charge density and electrostatic potential of a charged system at position z, respectively, and the superscript 0 denotes the uncharged equivalents. The plots only show the region near the surface as there is no difference in potential with a change in surface charge beyond that region for all systems (cf. SI Fig. 12). The first peak in all systems, located at 0 Å distance, corresponds to the change in charge of the surface platinum atoms. The charge densities for systems with 5000 and 9000 added water molecules are overall similar with slight differences in peak heights. In the case of 1000 added water molecules, differences compared to the uncharged case are only visible within a distance of less than 4 Å from the surface. An inflection point showing a shift in atomic positions is present in the charge density plots for all systems at ~2.5 Å. These inflection points indicate a shift of the adsorbed species either towards or away from the surface. For simulations with 5000 and 9000 added water molecules, an additional inflection point occurs at ~5 Å that represents the second adsorption layer. These charge-density profiles match the classical-electrostatic response, where a compact-layer structure of adsorbed ions and solvent molecules (cf. Figs. 8, 15), in which the electrostatic potential changes sharply, resides at the catalyst. This region is followed by a screening region, denoted by the second peak, where water reorientation and hydronium redistribution compensate the applied surface charge leading to the gradual decay in the electrostatic potential.

To gain a clear picture of the effect of the added surface charge on the properties of the electrolyte, we utilise the centre of molecular excess charge (COQ^{xs}_{mol}). The basis for this is the centre of charge that is a well-established concept in the literature, with the generalisation to the ionic charges similar to the capacitive compactness [54,55]. To calculate the COQ^{xs}_{mol}, the following equation is used

$$COQ^{xs}_{mol} = \frac{\int \left(\rho^{chg}_{mol}(z) - \rho^{0}_{mol}(z)\right) \cdot z\, dz}{\int \left(\rho^{chg}_{mol}(z) - \rho^{0}_{mol}(z)\right) dz}, \tag{7}$$

where z is the distance from the platinum surface, $\rho^{chg}_{mol}(z)$ and $\rho^{0}_{mol}(z)$ are the molecular charge densities, i.e., without considering the platinum atoms, averaged over the X-Y-plane at position z of the charged and uncharged systems, respectively. By plotting the resulting centre positions against the surface charge, the shift of the molecular excess charge can be tracked. Fig. 13 shows that the COQ^{xs}_{mol} converges to a similar value for all systems as along the branch of negative surface charge as the absolute charge increases. On the branches for the positive surface charges, this convergence is not observed. Notably, the sign of the surface charge at which the centre is closest to the platinum surface is different depending on the water content. In the case of 5000 and 9000 added water molecules the COQ^{xs}_{mol} is closest to the surface for positive charges. For the system with 1000 added water molecules, the

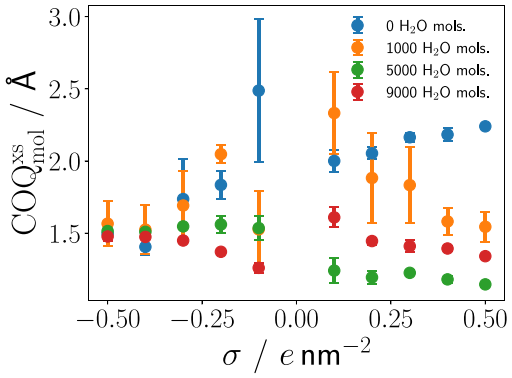


Fig. 13. Centres of molecular excess charge (cf. Eq. (7)) per water content with respect to surface charge.

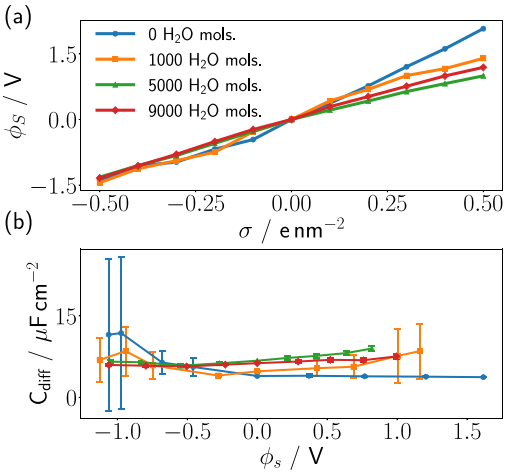


Fig. 14. (a) Electric surface potentials ϕ_s as a function of surface charge for each water content. The potential reference is chosen such that the uncharged systems have ϕ_s=0. (b) Differential capacitances C_{diff} as a function of electric surface potential for each water content. Calculated using Eq. (4) using neighbouring charge steps and ϕ_s values as described in Section 2.2.

positions are equal for positive and negative surface charges within the respective errors. For zero added water the closest position is observed for negative charges.

The electrostatic potential plots shown in the second column in Fig. 12 for the systems with 5000 and 9000 added water molecules are very similar, with only minute differences in peak heights. One structural difference between these two systems is the presence of sulfonic acid head groups that are adsorbed to the surface when 5000 water molecules were added. The different peak heights can most likely be attributed to the change in electrostatic interaction between these sulfonic acid head groups and the charged surface.

In the systems where no water has been added, the potential plots of the simulations with negatively charged surfaces are overlapping to a higher extent than those of positively charged surface systems. As a result, the spreads of electric surface potentials for negative and positive surface charges deviate greatly. This kind of deviation in magnitude of ϕ_s between the opposing surface charges is also observed in all other systems, however, in these simulations the larger magnitude is observed when the surface is negatively charged. When plotting ϕ_s against the surface charge, as shown in Fig. 14(a), we thus observe asymmetry in the plots for negative and positive values of σ. It is reminded that, for each system, the zero potential reference was chosen to correspond to the respective uncharged surface state (i.e., the PZC which is ~0.23 V vs. SHE) [40]. The relation of the plots to one another closely matches the relation observed in Fig. 13.

In Fig. 14(b), the differential capacitances, calculated with Eq. (4), are shown. The respective values are in the range of 4–12 μF cm^{-2}, which is comparable to the values obtained when using the data of Zhang et al., who had performed simulations using a ~2.5 nm thick hydrated Nafion film [25]. The plot shows asymmetric behaviour that changes with increased water content. Starting from the simulations with no water, we observe a maximum on the negative potential side and a plateau on the positive side. Once water is introduced, the negative side of the capacitance plot tends towards a plateau and the positive side shows a positive slope.

As the differential capacitance shows how the electrostatic potential changes due to changes in the applied surface charge, and the electrostatic potential is derived from the charge density, Fig. 14(b) gives an indication for the restructuring of the interfacial region upon adding water and varying the electrode potential. To elucidate this restructuring, we show the change in Z densities of the oxygen atoms of the hydronium and water molecules in Fig. 15, as these species are the only species that differ significantly when changing the surface charge. As already discussed for the uncharged reference, hydronium ions are strongly adsorbed to the surface yielding a large peak near the surface that accounts for ~70% of the hydronium ions, a value that is not justified by DFT reference. This overestimation of hydronium adsorption alters their distribution within the water phase. As a result changes in the distribution due to changes in the platinum charging state are not accurately represented in the differential capacitance. The stronger adsorption of water molecules that has also been identified in Section 3.1 is however systematic in all simulations and has only minor influence on the differential capacitance. Once the surface charge of the platinum slab is altered, the peak either de- or increases depending on the sign of the surface charge when hydronium ions are deleted or added, respectively. For the systems with 0 or 1000 added water molecules, the plots are very similar; however, as more water is added, a second peak appears at ~5 Å but only if the surface is negatively charged, i.e., for added hydronium ions. The stable second layer is formed once 30 or more hydronium ions are added, corresponding to surface charges of −0.3 e nm^{-2} or below. Thus, the presence of the second adsorption layer can be ascribed to crowding effects in the first adsorption layer of the hydronium molecules, which alters the chemical potential of the hydronium ions in that region. This may stem, for example, from the growth of electrostatic attraction of the water molecules in the first adsorption layer with the surface. As a result, the energy penalty for water desorption increases, which in turn prevents the exchange of water for hydronium ions into the first adsorption layer. With the second ion adsorption layer, the electric double layer thickness increases, causing the differential capacitance to decrease in the negative potential region. This trend from overscreening towards crowding in the adsorption layer at higher potentials, corresponding to higher surface charges, matches predictions by continuum theory [56]. For the positive potentials the observation is opposite to that for negative potentials. Here, the differential capacitances increase when water is added to the system. The Nafion layer more closely approaches the platinum surface as the water content decreases. Sulfonate anions at the Nafion side-chains will accumulate near the Pt surface at lower water content and in the region of positive surface charge density, leading to a reduction of the differential capacitance.

The changes in the Z-density profiles of the water oxygen atoms, as shown in Fig. 15 (right), are monotonic to one another with no differing features as seen for the hydronium Z densities. The shifts of the water molecules, as indicated by the inflection point and the change in water orientation (cf. SI Fig. 13), may play a small role in the differential capacitance, but a large influence can be ruled out. The main influence is the amount of water present, which leads to the shift in magnitude of the differential capacitances. It has to be noted that due to the usage of fixed point charges located on the atom sites the delocalisation of the

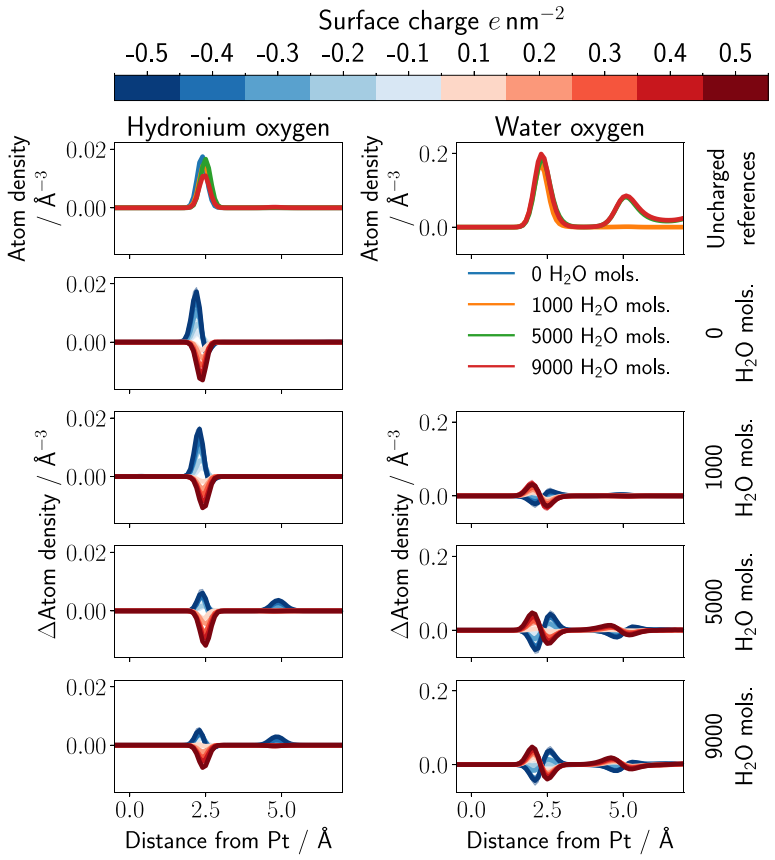


Fig. 15. Comparison of Z densities between uncharged and charged systems of hydronium oxygen (left) and water oxygen (right). Top row are references from the uncharged simulations for each water content. Rows 2–5 are differences in the occurrences of the specific atom species between the charged systems and the uncharged reference for 0, 1000, 5000 and 9000 added water molecules, respectively.

electronic charge distribution of the metal surface is not fully captured. As Ma et al. [57] have shown for a system of ionic liquid between charged electrodes, the use of a more sophisticated charge distribution, parametrised by joint density functional theory, lead to an increase in predicted differential capacitance compared to the atom centred results.

The electrostatic potential, and thus the differential capacitance, of the platinum-Nafion interface region is ultimately largely influenced by the amount and spatial distribution of hydronium ions. Due to the strong accumulation of hydronium ions near the platinum surface a large portion of the negative surface charge of the platinum is screened from the Nafion anionic groups, reducing the electrostatic repulsion between the negative platinum surface and anionic groups. With an added water film separating the Nafion from the surface, the differential capacitance curves are smoothed out as the restructuring is limited. These minimal changes are trackable by considering the COQ^{xs}_{mol}. With the large influence of hydronium adsorption, follow-up work is needed to scrutinise the adsorption behaviour.

4. Conclusion

We characterised the structural and electrostatic features of a catalyst–ionomer model interface constructed with a platinum (111) surface, varying degrees of water content and a Nafion thin film. A dense and relatively uniform Nafion thin film was generated by employing Voronoi tessellation. In this work we have identified crucial properties, such as the water film thickness, that are accessible with MD simulations. However, clear limitations, besides the inherent ones of using a classical force field and having finite simulation times, are seen as well that need to be addressed in follow-up work. These limitations include the overbinding of the hydronium ions, the fixed-charge treatment, the consideration of total system energies instead of free energies for the water-film thickness, and the sparse sampling of hydration levels.

For a specific parametric set-up used, a finite water film thickness between platinum and Nafion of less then 20 Å is energetically favoured. This value is however only a rough guide and it is not generalizable. The assessment needs to be refined by free energy calculations of finer hydration levels. Follow up simulations are planned to investigate this further. Nevertheless, this scale of water film thickness defines a nanoconfined interfacial phase, wherein the transport properties of the reactants are altered, directly impacting reaction kinetics. Given the proximity of the Nafion to the catalyst it not only acts as a proton conductor, but influences the local reaction environment and with that the electrochemical potentials of reactants. While the sulfonate groups of the Nafion may block adsorption sites for the reactants, their presence can also create microenvironments with enhanced dielectric screening, which can stabilise reaction intermediates and thereby lowering activation barriers.

In our electrostatic analysis we utilised the centre of molecular excess charge COQ^{xs}_{mol} as a means of tracking changes in the electrolyte due to added surface charge. These centres show correlation with the electrostatic potential, while providing additional insight into the structure of LRE. By computing the differential capacitances for systems with charged Pt surfaces, we observe peculiar trends in the charging behaviour around the PZC. We could identify changes in the accumulation of hydronium ions as the source of this behaviour. Another effect shaping the capacitance response will be the close possible approach of sulfonate anions to the platinum surface for systems with small water content.

Even in the uncharged case, a large portion of hydronium ions was found in close proximity of the surface, and by adding further ions into the system to balance the applied negative charge to the platinum surface, a second adsorption layer is formed. The presented workflow will be the basis for future studies employing more sophisticated methods to yield more detailed insights into the water film thickness, or for exploring metal-ionomer interfaces with PFAS-free ionomers. In the latter, the results obtained here will serve as reference to identify differences due to the change in the chemical nature of the ionomer. Follow-up work will need to address the effect of adsorbed hydrogen, hydroxide, and oxygen on the platinum surface, as is known from experiment [58,59], as well as reevaluate the force field in terms of adsorption strength of the hydronium ions.

CRediT authorship contribution statement

Dustin Vivod: Writing – original draft, Visualization, Validation, Methodology, Investigation, Formal analysis, Conceptualization. **Binny A. Davis:** Methodology, Formal analysis, Conceptualization. **Tobias Binninger:** Writing – review & editing, Supervision, Resources, Project administration. **Michael Eikerling:** Writing – review & editing, Supervision, Resources, Project administration, Funding acquisition.

Declaration of competing interest

The authors declare that they have no known competing financial interests or personal relationships that could have appeared to influence the work reported in this paper.

Acknowledgements

The authors gratefully acknowledge the Gauss Centre for Supercomputing e.V. (www.gauss-centre.eu) for funding this project by providing computing time through the John von Neumann Institute for Computing (NIC) on the GCS Supercomputer JUWELS at Jülich Supercomputing Centre (JSC). The authors acknowledge the financial support from the Federal Ministry of Science and Education (BMBF) under the German-Canadian Materials Acceleration Centre (GC-MAC) grant number 01DM21001A, and HIGHLANDER which receives funding from the Clean Hydrogen Partnership under grant agreement number 101101346.

Appendix A. Supplementary data

Supplementary material related to this article can be found online at https://doi.org/10.1016/j.electacta.2026.149933.

Data availability

Data will be made available on request.

References

[1] A. Kusoglu, A.Z. Weber, New insights into perfluorinated sulfonic-acid ionomers, Chem. Rev. 117 (3) (2017) 987–1104, http://dx.doi.org/10.1021/acs.chemrev.6b00159.

[2] T. Van Cleve, S. Khandavalli, A. Chowdhury, S. Medina, S. Pylypenko, M. Wang, K.L. More, N. Kariuki, D.J. Myers, A.Z. Weber, S.A. Mauger, M. Ulsh, K.C. Neyerlin, Dictating pt-based electrocatalyst performance in polymer electrolyte fuel cells, from formulation to application, ACS Appl. Mater. Interfaces 11 (50) (2019) 46953–46964, http://dx.doi.org/10.1021/acsami.9b17614.

[3] E. Panieri, K. Baralic, D. Djukic-Cosic, A. Buha Djordjevic, L. Saso, PFAS molecules: A major concern for the human health and the environment, Toxics 10 (2) (2022) http://dx.doi.org/10.3390/toxics10020044.

[4] R. Lohmann, I.T. Cousins, J.C. DeWitt, J. Glüge, G. Goldenman, D. Herzke, A.B. Lindstrom, M.F. Miller, C.A. Ng, S. Patton, M. Scheringer, X. Trier, Z. Wang, Are fluoropolymers really of low concern for human and environmental health and separate from other PFAS? Environ. Sci. Technol. 54 (20) (2020) 12820–12828, http://dx.doi.org/10.1021/acs.est.0c03244.

[5] A. Podder, A.A. Sadmani, D. Reinhart, N.-B. Chang, R. Goel, Per and polyfluoroalkyl substances (PFAS) as a contaminant of emerging concern in surface water: A transboundary review of their occurrences and toxicity effects, J. Hazard. Mater. 419 (2021) 126361, http://dx.doi.org/10.1016/j.jhazmat.2021.126361.

[6] E.S. Baker, D.R.U. Knappe, Per- and polyfluoroalkyl substances (PFAS)—contaminants of emerging concern, Anal. Bioanal. Chem. 414 (3) (2022) 1187–1188, http://dx.doi.org/10.1007/s00216-021-03811-9.

[7] T. Wang, Y. Zhang, B. Huang, B. Cai, R.R. Rao, L. Giordano, S.-G. Sun, Y. Shao-Horn, Enhancing oxygen reduction electrocatalysis by tuning interfacial hydrogen bonds, Nat. Catal. 4 (9) (2021) 753–762, http://dx.doi.org/10.1038/s41929-021-00668-0.

[8] R. Fan, S. Lu, F. Wang, Y. Zhang, M. Hojamberdiev, Y. Chai, B. Dong, B. Zhang, Enhancing catalytic durability in alkaline oxygen evolution reaction through squaric acid anion intercalation, Nat. Commun. 16 (1) (2025) 3407, http://dx.doi.org/10.1038/s41467-025-58623-7.

[9] Y. Zhou, K. Neyerlin, T.S. Olson, S. Pylypenko, J. Bult, H.N. Dinh, T. Gennett, Z. Shao, R. O'Hayre, Enhancement of Pt and Pt-alloy fuel cell catalyst activity and durability via nitrogen-modified carbon supports, Energy Env. Sci. 3 (2010) 1437–1446, http://dx.doi.org/10.1039/C003710A.

[10] C. Chen, H. Jin, P. Wang, X. Sun, M. Jaroniec, Y. Zheng, S.-Z. Qiao, Local reaction environment in electrocatalysis, Chem. Soc. Rev. 53 (2024) 2022–2055, http://dx.doi.org/10.1039/D3CS00669G.

[11] Z. Xu, X. Tan, C. Chen, X. Wang, R. Sui, Z. Zhuang, C. Zhang, C. Chen, Recent advances in microenvironment regulation for electrocatalysis, Natl. Sci. Rev. 11 (12) (2024) nwae315, http://dx.doi.org/10.1093/nsr/nwae315.

[12] X. Zhu, J. Huang, M. Eikerling, Hierarchical modeling of the local reaction environment in electrocatalysis, Acc. Chem. Res. 57 (15) (2024) 2080–2092, http://dx.doi.org/10.1021/acs.accounts.4c00234.

[13] X. Zhu, M. Eikerling, Coupled cation and pH effects in the hydrogen evolution reaction: An electrostati perspective, Curr. Opin. Electrochem. 57 (2026) 101852, http://dx.doi.org/10.1016/j.coelec.2026.101852.

[14] S.A. Berlinger, A. Chowdhury, T. Van Cleve, A. He, N. Dagan, K.C. Neyerlin, B.D. McCloskey, C.J. Radke, A.Z. Weber, Impact of platinum primary particle loading on fuel cell performance: Insights from catalyst/ionomer ink interactions, ACS Appl. Mater. Interfaces 14 (32) (2022) 36731–36740, http://dx.doi.org/10.1021/acsami.2c10499.

[15] D.L.I. Wood, J. Chlistunoff, J. Majewski, R.L. Borup, Nafion structural phenomena at platinum and carbon interfaces, J. Am. Chem. Soc. 131 (50) (2009) 18096–18104, http://dx.doi.org/10.1021/ja9033928.

[16] F. Chabot, J. Lee, F. Vandenberghe, L. Guétaz, G. Gebel, S. Lyonnard, L. Porcar, S. Rosini, A. Morin, Detailed catalyst layer structure of proton exchange membrane fuel cells from contrast variation small-angle neutron scattering, ACS Appl. Energy Mater. 6 (3) (2023) 1185–1196, http://dx.doi.org/10.1021/acsaem.2c02384.

[17] A. Nouri-Khorasani, K. Malek, A. Malek, T. Mashio, D.P. Wilkinson, M.H. Eikerling, Molecular modeling of the proton density distribution in a water-filled slab-like nanopore bounded by Pt oxide and ionomer, Catal. Today 262 (2016) 133–140, http://dx.doi.org/10.1016/j.cattod.2015.10.020.

[18] F. Chabot, P. Lionel, L. Guétaz, S. Rosini, A. Morin, Tracking the evolution of ionomer film and catalyst material to unravel PEMFC performance degradation, J. Electrochem. Soc. 171 (12) (2024) 124506, http://dx.doi.org/10.1149/1945-7111/ada111.

[19] V.M. Fernández-Alvarez, K. Malek, M.H. Eikerling, A. Young, M. Dutta, E. Kjeang, Molecular dynamics study of reaction conditions at active catalyst-ionomer interfaces in polymer electrolyte fuel cells, J. Electrochem. Soc. 169 (2) (2022) 024506, http://dx.doi.org/10.1149/1945-7111/ac4db3.

[20] R.K.S.S. Vuppala, B.A. Chaedir, L. Jiang, L. Chen, M. Aziz, A.P. Sasmito, Optimization of membrane electrode assembly of PEM fuel cell by response surface method, Molecules 24 (17) (2019) http://dx.doi.org/10.3390/molecules24173097.

[21] S. Jiang, Q. Xiang, Z. Xie, N. Yang, J. Liu, L. Li, Z. Wei, Influence of the pt/ionomer/water interface on the oxygen reduction reaction: insights into the micro-three-phase interface, Chem. Sci. 15 (2024) 19290–19298, http://dx.doi.org/10.1039/D4SC06600F.

[22] T. Min, Q. Zhou, Effects of liquid water on transport in the catalyst layer of proton exchange membrane fuel cells, Front. Energy Res. Volume 11 - 2023 (2023) http://dx.doi.org/10.3389/fenrg.2023.1330124.

[23] J.I. Siepmann, M. Sprik, Influence of surface topology and electrostatic potential on water/electrode systems, J. Chem. Phys. 102 (1) (1995) 511–524, http://dx.doi.org/10.1063/1.469429.

[24] S.K. Reed, O.J. Lanning, P.A. Madden, Electrochemical interface between an ionic liquid and a model metallic electrode, J. Chem. Phys. 126 (8) (2007) 084704, http://dx.doi.org/10.1063/1.2464084.

[25] Y. Zhang, L. Fan, J. Wang, H. Deng, W. Shi, Q. Du, Z. Hou, K. Jiao, Enhanced oxygen transport in ionomer films on platinum electrodes via a local electric field, J. Mater. Chem. A 10 (2022) 21102–21111, http://dx.doi.org/10.1039/D2TA05667D.

[26] V.M. Fernández-Alvarez, K. Malek, M.H. Eikerling, A. Young, M. Dutta, E. Kjeang, Insights into structure and properties of catalyst-ionomer interfaces in a PEM fuel cell cathode from atomistic molecular dynamics simulations, Electrochim. Acta 524 (2025) 146076, http://dx.doi.org/10.1016/j.electacta.2025.146076.
[27] J.C. Jiménez-García, J.A. Olmos-Asar, E.A. Franceschini, M.M. Mariscal, Effect of nafion content and hydration level on the electrochemical area of a pt nanocatalyst in the triple-phase boundary, Phys. Chem. Chem. Phys. 23 (2021) 27543–27551, http://dx.doi.org/10.1039/D1CP03731E.
[28] Q. Xue, R. Zhang, D. Yang, B. Li, P. Ming, C. Zhang, Effect of ionomer content on cathode catalyst layer for PEMFC via molecular dynamics simulations and experiments, Int. J. Hydrog. Energy 47 (55) (2022) 23335–23347, http://dx.doi.org/10.1016/j.ijhydene.2022.05.122.
[29] D. Kim, J. Lim, J.H. Lee, J. Choi, S.H. Kwon, S.-D. Yim, Y.-J. Sohn, S.G. Lee, Investigation of effect of platinum nanoparticle shape on oxygen transport in PEMFC catalyst layer using molecular dynamics simulation, ACS Omega 8 (35) (2023) 31801–31810, http://dx.doi.org/10.1021/acsomega.3c02886.
[30] J. You, H. Li, Y. Feng, X. Cheng, L. Luo, D. Yang, G. Wei, S. Shen, X. Yan, J. Zhang, Insight into oxygen diffusion mechanism in ionomer film on catalyst surface with varying perfluorosulfonic acid and water contents, J. Mater. Chem. A 12 (2024) 7248–7256, http://dx.doi.org/10.1039/D3TA07822A.
[31] J.C. Jiménez-García, D.F. Robledo Flores, R.H. Acosta, M.I. Velasco, E.A. Franceschini, M.M. Mariscal, Water behavior at PEMFC triple phase boundary: Exploring ionomer and catalytic layer effects via molecular dynamic simulations and NMR experiments, Int. J. Hydrog. Energy 52 (2024) 65–71, http://dx.doi.org/10.1016/j.ijhydene.2023.10.097.
[32] M. Rayhani, C. Jian, A review of molecular dynamic simulation on polymer electrolyte membrane fuel cell, J. Power Sources 657 (2025) 238143, http://dx.doi.org/10.1016/j.jpowsour.2025.238143.
[33] A.P. Thompson, H.M. Aktulga, R. Berger, D.S. Bolintineanu, W.M. Brown, P.S. Crozier, P.J. in 't Veld, A. Kohlmeyer, S.G. Moore, T.D. Nguyen, R. Shan, M.J. Stevens, J. Tranchida, C. Trott, S.J. Plimpton, LAMMPS - a flexible simulation tool for particle-based materials modeling at the atomic, meso, and continuum scales, Comp. Phys. Comm. 271 (2022) 108171, http://dx.doi.org/10.1016/j.cpc.2021.108171.
[34] T. Mabuchi, T. Tokumasu, Effect of bound state of water on hydronium ion mobility in hydrated Nafion using molecular dynamics simulations, J. Chem. Phys. 141 (10) (2014) 104904, http://dx.doi.org/10.1063/1.4894813.
[35] G.F. Brunello, J.H. Lee, S.G. Lee, J.I. Choi, D. Harvey, S.S. Jang, Interactions of pt nanoparticles with molecular components in polymer electrolyte membrane fuel cells: multi-scale modeling approach, RSC Adv. 6 (2016) 69670–69676, http://dx.doi.org/10.1039/C6RA09274H.
[36] R.W. Hockney, J.W. Eastwood, Computer Simulation Using Particles, Adam Hilger, Bristol, 1988.
[37] S.S. Jang, V. Molinero, T. Çagin, W.A. Goddard, Nanophase-segregation and transport in Nafion 117 from molecular dynamics simulations: Effect of monomeric sequence, J. Phys. Chem. B 108 (10) (2004) 3149–3157, http://dx.doi.org/10.1021/jp036842c.
[38] P. Virtanen, R. Gommers, T.E. Oliphant, M. Haberland, T. Reddy, D. Cournapeau, E. Burovski, P. Peterson, W. Weckesser, J. Bright, S.J. van der Walt, M. Brett, J. Wilson, K.J. Millman, N. Mayorov, A.R.J. Nelson, E. Jones, R. Kern, E. Larson, C.J. Carey, İ. Polat, Y. Feng, E.W. Moore, J. VanderPlas, D. Laxalde, J. Perktold, R. Cimrman, I. Henriksen, E.A. Quintero, C.R. Harris, A.M. Archibald, A.H. Ribeiro, F. Pedregosa, P. van Mulbregt, SciPy 1.0 Contributors, SciPy 1.0: Fundamental algorithms for scientific computing in python, Nature Methods 17 (2020) 261–272, http://dx.doi.org/10.1038/s41592-019-0686-2.
[39] X. Lin, S.R. Tee, D.J. Searles, P.T. Cummings, Molecular insights on optimizing nanoporous carbon-based supercapacitors with various electrolytes, Electrochim. Acta 474 (2024) 143500, http://dx.doi.org/10.1016/j.electacta.2023.143500.
[40] P. Xu, A.D. von Rueden, R. Schimmenti, M. Mavrikakis, J. Suntivich, Optical method for quantifying the potential of zero charge at the platinum–water electrochemical interface, Nat. Mater. 22 (4) (2023) 503–510, http://dx.doi.org/10.1038/s41563-023-01474-8.
[41] S.R. Tee, D.J. Searles, Constant potential and constrained charge ensembles for simulations of conductive electrodes, J. Chem. Theory Comput. 19 (10) (2023) 2758–2768, http://dx.doi.org/10.1021/acs.jctc.3c00153.
[42] N. Michaud-Agrawal, E.J. Denning, T.B. Woolf, O. Beckstein, MDAnalysis: A toolkit for the analysis of molecular dynamics simulations, J. Comput. Chem. 32 (10) (2011) 2319–2327, http://dx.doi.org/10.1002/jcc.21787.
[43] R.J. Gowers, M. Linke, J. Barnoud, T.J.E. Reddy, M.N. Melo, S.L. Seyler, J. Domański, D.L. Dotson, S. Buchoux, I.M. Kenney, O. Beckstein, MDAnalysis: A python package for the rapid analysis of molecular dynamics simulations, SciPy 2016 (2016) http://dx.doi.org/10.25080/Majora-629e541a-00e.
[44] W. Humphrey, A. Dalke, K. Schulten, VMD – visual molecular dynamics, J. Mol. Graph. 14 (1996) 33–38.
[45] J. Stone, An Efficient Library for Parallel Ray Tracing and Animation, Computer Science Department, University of Missouri-Rolla, 1998.
[46] S. Sakong, A. Groß, Water structures on a Pt(111) electrode from ab initio molecular dynamic simulations for a variety of electrochemical conditions, Phys. Chem. Chem. Phys. 22 (2020) 10431–10437, http://dx.doi.org/10.1039/C9CP06584A.
[47] R. Tesch, P.M. Kowalski, M.H. Eikerling, Properties of the Pt(111)/electrolyte electrochemical interface studied with a hybrid DFT–solvation approach, J. Phys.: Condens. Matter. 33 (44) (2021) 444004, http://dx.doi.org/10.1088/1361-648X/ac1aa2.
[48] S. Sakong, A. Groß, The electric double layer at metal-water interfaces revisited based on a charge polarization scheme, J. Chem. Phys. 149 (8) (2018) 084705, http://dx.doi.org/10.1063/1.5040056.
[49] D. Fraggedakis, Theory of ion chemical potentials in heterogeneous electrolyte environments, J. Chem. Phys. 164 (12) (2026) 124705, http://dx.doi.org/10.1063/5.0319762.
[50] S.A. Berlinger, B.D. McCloskey, A.Z. Weber, Probing ionomer interactions with electrocatalyst particles in solution, ACS Energy Lett. 6 (6) (2021) 2275–2282, http://dx.doi.org/10.1021/acsenergylett.1c00866.
[51] D.J. Bonthuis, S. Gekle, R.R. Netz, Dielectric profile of interfacial water and its effect on double-layer capacitance, Phys. Rev. Lett. 107 (2011) 166102, http://dx.doi.org/10.1103/PhysRevLett.107.166102.
[52] D.J. Grzetic, K.T. Delaney, G.H. Fredrickson, Contrasting dielectric properties of electrolyte solutions with polar and polarizable solvents, Phys. Rev. Lett. 122 (2019) 128007, http://dx.doi.org/10.1103/PhysRevLett.122.128007.
[53] M. Kanduč, A. Schlaich, E. Schneck, R.R. Netz, Water-mediated interactions between hydrophilic and hydrophobic surfaces, Langmuir 32 (35) (2016) 8767–8782, http://dx.doi.org/10.1021/acs.langmuir.6b01727.
[54] N. Luque, W. Schmickler, The electric double layer on graphite, Electrochim. Acta 71 (2012) 82–85, http://dx.doi.org/10.1016/j.electacta.2012.03.083.
[55] G.I. Guerrero-García, E. González-Tovar, M. Chávez-Páez, J. Kłos, S. Lamperski, Quantifying the thickness of the electrical double layer neutralizing a planar electrode: the capacitive compactness, Phys. Chem. Chem. Phys. 20 (2018) 262–275, http://dx.doi.org/10.1039/C7CP05433E.
[56] M.Z. Bazant, B.D. Storey, A.A. Kornyshev, Double layer in ionic liquids: Overscreening versus crowding, Phys. Rev. Lett. 106 (2011) 046102, http://dx.doi.org/10.1103/PhysRevLett.106.046102.
[57] J. Ma, S. Zhao, Z. Li, New crowding states of ionic liquid induced by configuration change of ion adsorption on charged electrode, Electrochim. Acta 425 (2022) 140692, http://dx.doi.org/10.1016/j.electacta.2022.140692.
[58] A.M. Gómez-Marín, J. Clavilier, J.M. Feliu, Sequential Pt(111) oxide formation in perchloric acid: An electrochemical study of surface species inter-conversion, J. Electroanal. Chem. 688 (2013) 360–370, http://dx.doi.org/10.1016/j.jelechem.2012.07.016.
[59] R. Rizo, E. Herrero, V. Climent, J.M. Feliu, On the nature of adsorbed species on platinum single-crystal electrodes, Curr. Opin. Electrochem. 38 (2023) 101240, http://dx.doi.org/10.1016/j.coelec.2023.101240.